NATIONAL UNIVERSITY OF SCIENCE AND TECHNOLOGY POLITEHNICA BUCHAREST

Doctoral School of Engineering and Applications of Lasers and Accelerators

Decision No. .... from .....-.....-........

Ph.D. THESIS

Teodora Andreea (MADGEARU) PETRUSE

SUMMARY

THE COMMISSIONING OF ELISSA DETECTION ARRAY AND THE MEASUREMENT OF FLUORINE FOR AGB STELLAR NUCLEOSYNTHESIS

THESIS COMMITTEE

Prof. Dr. Ing. Călin A. Ur Politehnica Bucharest, IFIN-HH/ELI-NP	President
Prof. Dr. Dimiter L. Balabanski Politehnica Bucharest, IFIN-HH/ELI-NP	PhD Supervisor
Prof. Dr. Cătălin Matei Politehnica Bucharest, IFIN-HH/ELI-NP	Referee
Prof. Dr. Aurora Tumino University Kore Enna, INFN-LNS	Referee
Prof. Dr. Mihaela Sin University of Bucharest	Referee

BUCHAREST 2024

Acknowledgements

I am deeply thankful to my PhD coordinator, Dr. Dimiter Balabanski for his guidance and constant encouragement. I would like to express my sincere gratitude to the Extreme Light Infrastructure Sillicon Strip Array group, and in particular to its head, Dr. Catalin Matei, for providing an inspiring and stimulating research environment.

I am grateful to our foreign collaborators. I would like to extend particular thanks to Dr. Dario Lattuada and, especially, to Dr. Luca Guardo, whose expertise and support were instrumental to the success of this thesis. Without his magic, this thesis would not have been possible.

I would like to thank my colleagues from Extreme Light Infrastructure - Nuclear Physics, namely the Gama Driven Experiments Department, for their invaluable support and collaboration throughout this research journey.

I am forever grateful to my family and friends for their constant trust and support. My in-laws, Tudor, Andra, my parents, Mariana and Romulus, and my sister, Malina, have been a constant source of strength.

My deepest gratitude goes to my husband, Andrei, whose love and support have been immeasurable. This thesis is dedicated to my beloved daughters, Sofia and Ilinca. Their presence has brought immense joy to my life, although they may have unintentionally extended this journey. Their love and laughter have made every challenge worthwhile.

Abstract

The ^{19}F(p,α)^{16}O reaction is crucial in stellar nucleosynthesis, being the primary fluorine destruction channel in hydrogenrich environments. However, current models overpredict fluorine abundances in AGB stars, suggesting the need for better experimental data. The reaction proceeds through (p,α_0), (p,α_π), and (p,α_γ) channels, with channel dominance depending on temperature. Experimental data for this reaction at astrophysically relevant energies is limited due to the Coulomb barrier. Extrapolations from higher energy data are used, but a more precise understanding is needed for low temperatures.

The ELISSA detector array was developed to measure charged particles from photodissociation reactions. It was tested at the 3 MV Tandetron accelerator. This thesis presents a characterization of the ELISSA setup, including energy and position resolution, and comparison of DAQ systems and electronic chains.

The $^{19}F(p,\alpha_0)^{16}$O reaction cross section was studied between 400 keV and 900 keV center-of-mass energy. Our results resolve discrepancies in previous data and provide new insights into the reaction.

The $^{19}F(p,\alpha_\pi)^{16}$O anf $^{19}F(p,\alpha_\gamma)^{16}$O reaction cross sections were studied between 300 keV and 700 keV center-of-mass energy with ELISSA detector array. The reaction channel of interest can be selected due to the performance of the experimental setup.

Table of contents

List of tables

List of figures

Introduction

In this work, I studied the $^{19}F(p,\alpha_0)^{16}O$ reaction cross section from 400 keV to 900 keV, solving the discrepancies in the previous data sets in the literature. I also studied $^{19}F(p,\alpha_\pi)^{16}O$ and $^{19}F(p,\alpha_\gamma)^{16}O$ in the 300-700 keV range. The thesis is divided into five chapters: the first two represent the theoretical aspects concerning AGB stellar nucleosynthesis and stellar thermonuclear reaction rates.

Most elements are synthesized in from stars. Heavier elements are produced through neutron capture, with the *s*-process creating elements from iron to lead in low-mass AGB stars. AGB stars also produce fluorine. Fluorine abundance is used to study AGB stars, but current models cannot fully explain it due to uncertainties in reaction rates, mixing processes, and nucleosynthesis near the convective envelope.

This work focuses on the $^{19}F(p,\alpha)^{16}O$ reaction, the primary fluorine destruction mechanism in AGB stars. It occurs through (p,α_0), (p,α_π), and (p,α_γ) channels.

Experimentally determining reaction rates at astrophysical energies is difficult due to the exponential decrease of the cross section at low energies and electron screening effects.

The next tree chapters of the thesis represent my original work. Chapter tree describes the ELISSA silicon strip detector array, which was developed for nuclear astrophysics experiments at ELI-NP. It's designed to measure charged particles emitted in photodisintegration reactions. We present the experimental setup, data acquisition system, and initial characterization of the ELISSA array. Results on energy resolution and position reconstruction demonstrate its suitability for nuclear astrophysics studies at ELI-NP. ELISSA detection array was also fully characterized in-beam. The commissioning experiment is further detailed in the thesis. Its performance and potential for particle identification were expoled.

In chapter four the new experimental data for the $^{19}F(p,\alpha_0)^{16}O$ reaction cross section in the center-of-mass energy region of 400-900 keV using the LHASA silicon strip detector setup is presented. The extracted angular distributions and calculated *S*factors are compared with previous measurements solving the discrepancies in the literature.

Chapter five presents new experimental data for the $^{19}F(p,\alpha_\pi)^{16}O$ and $^{19}F(p,\alpha_\gamma)^{16}O$ reaction cross section in the center-of-mass energy range of 300-700 keV using the ELISSA silicon strip detector array. Due to ELISSA detector's energy resolution, the two channels of interest can be separated anf this recations can be studied.

Chapter 1

AGB stellar evolution and nucleosynthesis

1.1 Abundances in the solar system

Most elements formed in stars, with exceptions being hydrogen, helium, and trace amounts of lithium. Elements heavier than iron are produced through neutron capture processes. The solar system's abundance distribution shows a decreasing trend from lighter to heavier elements. Most mass is in hydrogen and helium (Figure 1.1).
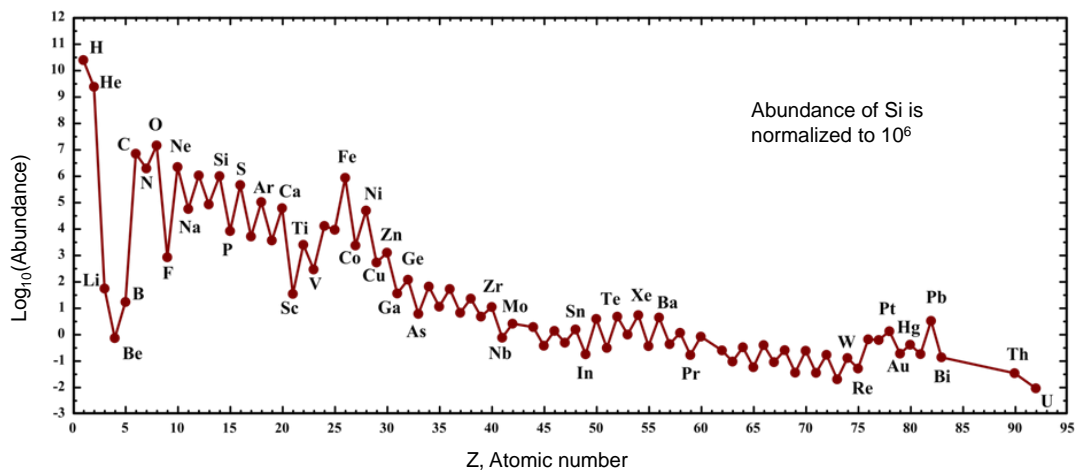
Figure 1.1 The present nuclear abundance pattern found in our solar system; taken from [1].

Elements heavier than ^{12}C are synthesized within stars. Charged-particle nuclear reactions in different stellar burning stages produce elements between ^{12}C and ^{40}Ca. The Coulomb barrier decreases the probability of these reactions to occur, leading to the decreasing abundance curve.

The iron peak, where abundance is maximum, corresponds to the highest binding energy per nucleon. Beyond iron, neutron capture processes produce heavier elements

due to the Coulomb barrier. Burbidge *et al.* [2] proposed the *s*-process and *r*-process for producing heavy elements. The *s*-process occurs in low neutron-density environments in AGB stars. The *r*-process occurs in neutron-rich conditions, typically associated with explosive stellar events. The *s*-process is responsible for synthesizing approximately half of the elements heavier than iron. AGB stars are key sites for *s*-process nucleosynthesis, where neutron-rich material is produced and brought to the stellar surface through convective mixing.

1.2   Evolution of the AGB phase

A star's evolution is determined by its initial mass, internal structure, and energy generation processes. These changes are measured as surface temperature and luminosity, plotting the star's trajectory on the Hertzsprung-Russell (HR) diagram (Figure 1.2).
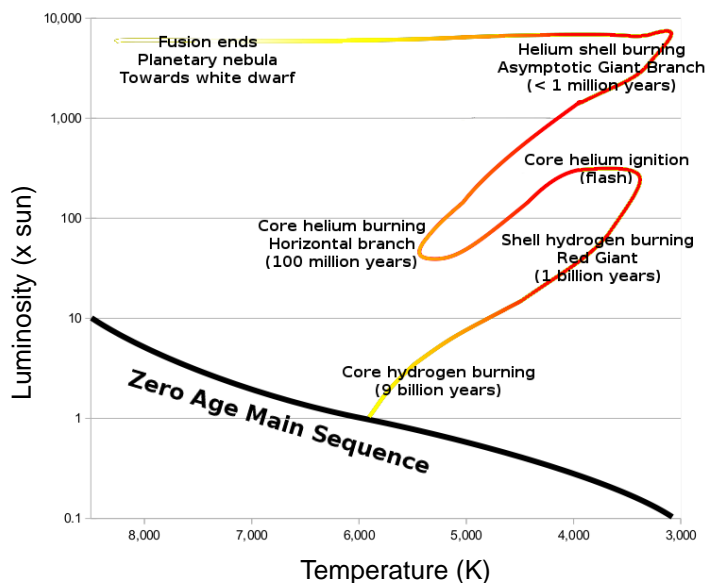
Figure 1.2 The stellar evolution as a function of luminosity and temperature (HR diagram); taken from [3].

Stars begin on the Zero-Age Main Sequence (ZAMS) [4], where core hydrogen fusion starts. Hydrogen fusion proceeds through the proton-proton (pp) chain or the carbon-nitrogen-oxygen (CNO) cycle. The pp chain converts hydrogen into helium. The CNO cycle converts hydrogen into helium using carbon, nitrogen, and oxygen as catalysts.

After core hydrogen exhaustion, a star leaves the main sequence, transitioning to the Red Giant Branch (RGB). The core contracts, while outer layers expand and cool, becoming convective. This marks the transformation of the star into the RGB [5].

As a result of the insufficient energy for carbon-oxygen fusion, the core starts to contract due to the gravitational force. The heat coming from core contractions is transferred to the surrounding layer, therefore ignition of shell helium starts. At this stage the core is composed of carbon, oxygen and small quantities of neon. In this phase, a star will transition from the RGB to AGB phase (Figure 1.2). The AGB derives its name from its asymptotic approach to the RGB. At this stage, the star contains a H-rich outer convective envelope. As we go towards the core of the star, we can find a H-burning shell, which is followed by an intert He intershell. Directly above the core, there is a He-burning shell, while the core itself is a degenerate CO core [6].

1.2.1   The Thermally Pulsing AGB phase

A thermal pulse has distinct phases: ignition, peak energy release, power-down, dredge-up, and return to an inactive state. Enough He accumulation triggers the initial thermal pulse. This leads to compression, heating, and He ignition. The intense energy output results in a pulse-driven convective zone (PDCZ) reaching from the helium-burning layer to the hydrogen-rich envelope. This mixing of elements allow the synthesis of *s*-process elements and fluorine.

1.3   Neutron capture process

Neutron capture is the primary process for synthesizing elements heavier than iron. The equation for neutron capture is:

$$_{Z}^{A}X + n \rightarrow _{Z}^{A+1}X + \gamma \tag{1.1}$$

If the resulting nucleus $_{Z}^{A+1}X$ is stable, another neutron will be captured, forming $_{Z}^{A+2}X$. If it is unstable, its neutron capture timescale (τ_n) must be compared to its β-decay timescale (τ_β). β decay can occur through two modes:

$$\beta^+ decay :_{Z}^{A+1}X \rightarrow _{Z-1}^{A+1}Y + e^+ + \nu_e \tag{1.2}$$

$$\beta^- decay :_{Z}^{A+1}X \rightarrow _{Z+1}^{A+1}Y + e^- + \nu_e \tag{1.3}$$
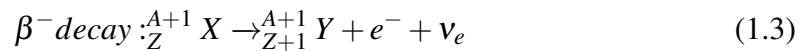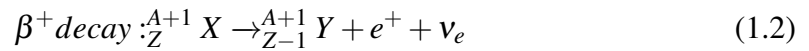
Neutron capture nucleosynthesis occurs through the following scenarios:

- Slow *s*-process - β-decay dominates neutron capture. Stable or long-lived isotopes lead to heavier elements. This process occurs in lower neutron density environments and follows a path along the valley of beta stability, ending at ^{209}Bi.

- Rapir *r*-process - Neutron capture dominates β decay. Requires high neutron densities and temperatures, found in explosive environments. Neutron-rich isotopes

accumulate until β-decay dominates. Unstable nuclei decay to achieve stable configurations.

1.4   AGB stellar nucleosynthesis

1.4.1   The *s*-process nucleosynthesis

Identifying the primary neutron supplier for the *s*-process is challenging. Possible reactions were ^{13}C(α, n)^{16}O and ^{21}Ne(α, n)^{24}Mg [7], both active during helium burning. These sources lead to varying elemental abundance patterns. ^{13}C(α, n)^{16}O becomes active around T = 0.9 x 10^8 K, while ^{22}Ne is efficient in hotter environments of intermediate-mass AGB stars. It was proposed ^{14}N(α, γ)^{18}F(β^+)^{18}O(α, γ)^{22}Ne(α, n)^{25}Mg as a possible neutron source. Finding the main neutron source inside stars is not trivial.

1.4.2   Nucleosynthesis of Fluorine

The origins of ^{19}F have long captivated scientists. Three primary astrophysical sites for ^{19}F production are proposed:

- Core-Collapse Supernovae: Woosley and Haxton (1988) [8] suggested that neutrino dissociation of ^{20}Ne within collapsing massive star cores could generate ^{19}F, potentially ejecting it into the interstellar medium before destruction. Neutrino-nucleus reactions, despite having small cross-sections, become significant due to the very high neutrino flux released during core collapse to a neutron star (ν-process).

- Wolf-Rayet Stars: Meynet and Arnould (2000) [9] proposed an alternative scenario where massive stars, specifically Wolf-Rayet stars, might synthesize ^{19}F through He burning and subsequently expel it in the interstellar space *via* powerful stellar winds.

- Asymptotic Giant Branch (AGB) Stars: The first observational evidence for ^{19}F production in AGB stars emerged in 1992, with Jorissen and Arnould [10] detecting hydrogen fluoride (HF) features in their spectra. Their findings revealed a correlation between high C/O ratio and ^{19}F abundance in AGB stars, suggesting a link between carbon enrichment and ^{19}F production on the stellar surface.

The dominant contributor to the ^{19}F abundance remains a source of ongoing investigation. Given this uncertanties in the ^{19}F production site, it is mandatory to further study, both theoretically and experimentally the production mechanisms of this element, as well as its abundance in the Universe.

Chapter 2

Reaction rates within stars

Stellar interiors depend on thermonuclear reactions for energy generation and nucle-
osynthesis. Thermal motion governs these reactions. Various thermonuclear reaction
sequences occurring at distinct stellar evolution stages produce heavier elements. This
chapter explores the theory and methodologies used to determine nuclear reaction rates
within stars.

2.1 Reaction rates

Thermonuclear reactions involve two particles: a projectile and a target nucleus [2]. The
reaction releases or absorbs energy based on the change in rest mass. Stellar burning
relies on exoenergetic thermonuclear reactions. The reaction rate is proportional to the
cross section (σ), which represents the probability of a successful interaction between
the reacting nuclei. Considering a stellar plasma composed of two particles, the reaction
rate per unit volume (r) is:

$$r = N_X N_a v \sigma(v) \tag{2.1}$$

where N_X and N_a are particle densities, v is relative velocity, and $\sigma(v)$ is the reaction
cross section. The average reaction rate is [11]:

$$< \sigma v >= \int_0^\infty \phi(v) v \sigma(v) dv \tag{2.2}$$

where ϕ(v) is the relative velocity distribution. The overall reaction rate is:

$$r = N_X N_a < \sigma v > (1 + \delta_{Xa})^{-1} \tag{2.3}$$

where δ_{Xa} is the Kroneker delta. It equals 1 when the particles are identical, and 0 other-
wise [12]. In stellar environments, particle velocities follow the Maxwell-Boltzmann
distribution law:

$$\phi(v) = 4\pi v^2 \left(\frac{m}{2\pi k_B T} \right)^{\frac{3}{2}} e^{-\frac{mv^2}{2k_B T}} \tag{2.4}$$

where k_B is Boltzmann's constant and T the gas temperature.

For exoenergetic reactions, no minimum energy is necessary. For endothermic reactions, a minimum energy threshold is required.

2.1.1 Penetration through Coulomb barrier and the astrophysical S-factor

The reaction cross section reflects the likelihood of particles interacting. Measuring the cross section helps understand reaction rates in a stellar plasma. Determining the cross section is crucial for understanding stellar energy production and elemental abundance. The Coulomb barrier is a significant challenge in measuring cross sections. It arises from the electrostatic repulsion between charged particles, decreasing the probability of nuclear reactions to happen [13]. Figure 2.1 shows a visual representation of the Coulomb potential.
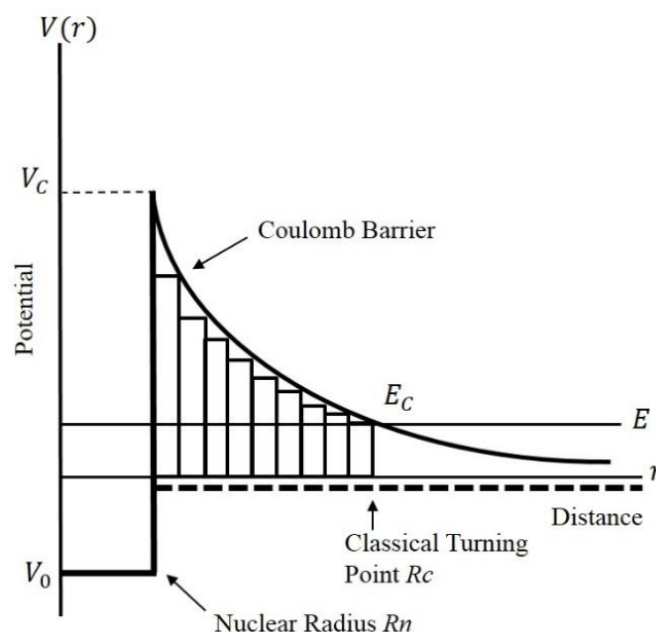
Figure 2.1 Representation of the Coulomb barrier; the figure is taken from [14].

$$V = \frac{Z_1 Z_2 e^2}{r} \tag{2.5}$$

The closest approach (r_C) occurs when the projectile's total energy (E) equals the Coulomb barrier peak (V_C). Projectiles with sufficient energy can overcome this barrier and undergo nuclear reactions. Fusion reactions involving heavier nuclei require higher energies to overcome the stronger Coulomb repulsion. This translates to higher temperatures for fusion of heavier elements.

Quantum mechanical tunneling allows nuclei to penetrate the Coulomb barrier with
a finite probability [14], described by [12]:

$$P_l = \frac{|\chi_l(\infty)|^2}{|\chi_l(R)|^2} \tag{2.6}$$

where $|\chi_l(\infty)|^2$ and $|\chi_l(R)|^2$ describe the probability that the particles are found at the
interaction radius, respectively at r_C.

The radial part of the Schrödinger equation is:

$$\frac{d^2\chi_l}{dr^2} + \frac{2\mu}{\hbar^2}[E - V_l(r)]\chi_l = 0 \tag{2.7}$$

The solutions are the regular Coulomb wave function ($F_l(r)$) and the irregular Coulomb
wave function ($G_l(r)$).

The penetration probability for the s-wave (l=0) component is:

$$P_0 = e^{-2\pi\eta} \tag{2.8}$$

where η is the Sommerfeld parameter:

$$\eta = \frac{Z_1 Z_2 e^2}{\hbar v} \tag{2.9}$$

The Gamow energy is:

$$E_G = 2\mu(\pi v \eta)^2 \propto (Z_1 Z_2)^2 \mu MeV \tag{2.10}$$

The Sommerfeld parameter (η) indicates the strength of the Coulomb interaction. It's
directly proportional to the product of the interacting ions charges but inversely propor-
tional to the kinetic energy. The cross section is approximately:

$$\sigma(E) \propto \frac{1}{E}e^{-2\pi\eta} \tag{2.11}$$

The S-factor is introduced to remove the energy dependence of the cross section:

$$S(E) = \sigma(E)E e^{2\pi\eta} \tag{2.12}$$

$$\sigma(E) = \frac{1}{E}S(E)e^{-2\pi\eta} \tag{2.13}$$

It is clar from Figure 2.2 that the S-factor shows a reduced dependence on beam energy,
facilitating extrapolation to astrophysical energies.
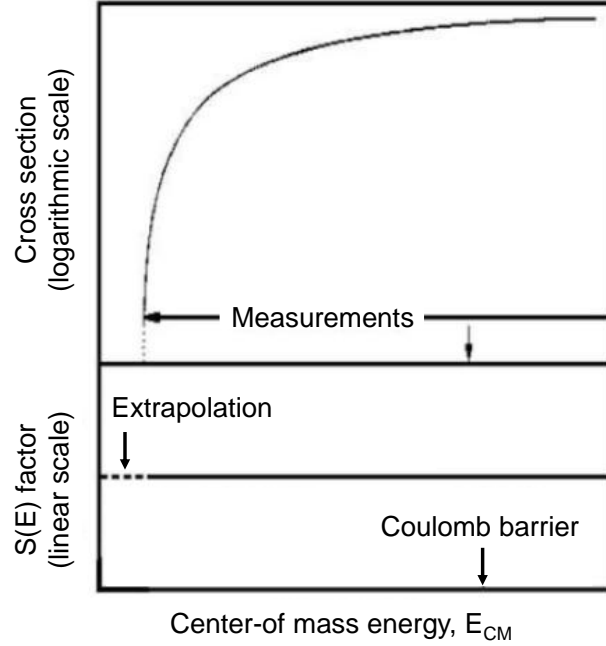
Figure 2.2 The dependence of the σ, respectively S-factor on the center-of-mass energy; figure taken from [11].

2.1.2 Non-resonant reaction rates

The astrophysical S-factor is an essential tool for obtaining an analytical formula describing the reaction rate in non-resonant scenarios.

$$< \sigma v >= \left(\frac{8}{\pi\mu}\right)^{\frac{1}{2}} \frac{1}{(k_BT)^{\frac{3}{2}}} \int_0^\infty \sigma(E)e^{-\frac{e}{k_BT}-(\frac{E_G}{E})^{\frac{1}{2}}} dE \qquad (2.14)$$

The integrand has two exponential terms:

- $e^{-\frac{E}{k_BT}}$ is significant for low energies;

- $e^{-\frac{E_G}{E}}$ is relevant at higher energies.

Multiplying these terms results in a peak of the function integral called the Gamow peak, situated at energy value E_0.

In the absence of resonances, we assume a constant astrophysical S-factor within the narrow energy region around the Gamow peak [11]:

$$S(E) = S(E_0) = S_0 = constant \qquad (2.15)$$

In stars, the combined effect of temperature and the repulsive electrical force between nuclei creates the Gamow window. This window is centered around the effective burning energy (E_0) and represents the energy range where nuclear reactions occur most efficiently. The Gamow window shifts to higher energies as the density and temperature

of a star rise. The width of this window and the effective burning energy are given by:

$$E_0 = \left(\frac{k_B T}{2}\right)^{\frac{3}{2}} E_G^{\frac{1}{2}} = 1.22[(Z_1 Z_2)^2 \mu T_6^2]^{\frac{1}{3}} (keV) \tag{2.16}$$

$$\Delta = \frac{1}{3^{\frac{1}{2}}} (E_0 k_B T)^{\frac{1}{2}} = 0.749(Z_1^2 Z_2^2 \mu T_6^5)^{\frac{1}{6}} (keV) \tag{2.17}$$

A higher Coulomb barrier translates to a higher energy range for the Gamow window.

The fusion cross section at the Gamow energy is very small, ranging from 10^{12} to 10^9 barns. Directly measuring the cross section inside the Gamow window is extremely challenging. The current practice involves measuring the cross section in a broader energy range and then extrapolating the data down to the Gamow energy.

Resonant reactions involve the formation of a temporary, compound nucleus.

2.1.3 Resonant reaction rates

Resonant reactions occur when colliding nuclei form a compound nucleus. This process differs from direct capture, which occurs at any projectile energy. Resonant reactions are energy-dependent and occur when the combined energy of the entrance channel matches a specific excited state energy (resonance energy, E_r) in the compound nucleus.

The Breit-Wigner function [11] describes the behavior of resonant cross sections:

$$\sigma(E)_{BW} = \pi \lambda^2 \frac{2J+1}{(2J_x+1)(2J_a+1)} (1+\delta_{xa}) \frac{\Gamma_1 \Gamma_2}{(E-E_r)^2 + (\Gamma/2)^2} \tag{2.18}$$

where:

- λ is the de Broglie wavelength in the center-of-mass frame, determined by Planck's constant ($\hbar$), reduced mass (μ), and projectile energy (E);

- J_x denotes the spin of the projectile (X), J_a denotes the spin of the target (a) and J represents the angular momentum of the resonance;

- $(1+\delta_{xa})$ corrects for double-counting when identical particles are involved in the reaction;

- E_r is the resonance energy, distinct from the projectile energy (E);

- Γ_1 and Γ_2 represent the partial widths for the reaction's entrance channel and exit channel, characterizing the compound nucleus creation and destruction. The total width (Γ) represents the summing of all partial widths for accessible reaction channels.

By introducing the Breit-Wigner cross section in the reaction rate, the following relation emerges:

$$<\sigma v> = \left(\frac{8}{\pi\mu}\right)^{\frac{1}{2}} \frac{1}{(k_B T)^{\frac{3}{2}}} \int_0^\infty \sigma(E)_{BW} e^{-\frac{E}{k_B T}} dE \tag{2.19}$$

The mean lifetime of the quasistationary state of the compound nucleus is linked to the total width. Resonances with energies (E_r) close to $k_b T$ dominate the reaction rate.

For multiple narrow resonances, the total resonant reaction rate per particle pair is the sum of individual resonance contributions. For broad resonances, the partial widths energy dependence becomes significant. The low-energy part of a broad resonance exhibits a smooth energy dependence, allowing for treatment similar to non-resonant reactions. However, the S-factor at the Gamow energy is influenced by the resonance parameters. Subthreshold resonances can impact the S-factor within the astrophysically relevant energy range.

2.2 The problems of measurements at astrophysicaly relevant energies

Measuring reaction cross sections in the astrophysical region is challenging. Reactions occur around the Gamow peak, but the Coulomb barrier is significant. This leads to quantum mechanical tunneling and exponentially decreasing cross sections, making detection difficult.

The number of detected particles (N_{det}) depends on:

- Beam particle flux (N_{imp});

- Target particles (N_{tar});

- Detector angular coverage ($\Delta\Omega$);

- Detector efficiency (ε).

Increasing N_{det} has challenges:

- Higher beam current: Target heating, detector damage, elevated dead time;

- Thicker target: Increased energy loss and angular straggling;

- Larger detector solid angle: Electronics complexity and detector placement.

Electron screening effects can hinder accurate extraction of the astrophysical S-factor. Fitting high-energy data to a theoretical function and extrapolating to astrophysical energies can be unreliable.

Chapter 3

The development of ELISSA detection setup

3.1   Nuclear astrophysics at ELI-NP

Extreme Light Infrastructure - Nuclear Physics (ELI-NP) in Magurele, Romania, is a leading nuclear physics research facility. ELI is a pan-European infrastructure for high-power laser research. ELI-NP [15] utilizes high-power lasers and γ beams for fundamental nuclear physics research. Its two 10 PW lasers generate unprecedented intensities (up to 10^{23} - 10^{24} W/cm^2), and its high-brilliance γ-ray beam system features narrow bandwidth, tunable energy, and high linear polarization.

   The high-power lasers use Optical Parametric Chirped Pulse Amplification (OPCPA) technology. Each arm delivers pulses at three power levels: 10 PW, 1 PW, and 0.1 PW, with corresponding pulse repetition rates: 1/60 Hz, 1 Hz, and 10 Hz.

   The γ-ray beam at ELI-NP is produced through inverse Compton scattering. The VEGA system, composed of a LINAC and a storage ring, accelerates electrons and interacts them with laser photons in an optical cavity. The Gama Driven Experiments Department (GDED) at ELI-NP will utilize the γ-ray beam at different experimental setups. The VEGA gamma beam parameters are shown in Table 3.1 [16].

Table 3.1 Characteristics of the VEGA system

Quantity	Unit of measurement	Specification
Maximum Photon Energy	MeV	> 19.5
Tunability of the Photon Energy		Steplessly variable
Linear Polarization of Gamma-Ray Beam	%	> 95
Divergence at FWHM of Beam Spot	rad	$< 1.5 \ 10^{-4}$
Total Photon Flux		$> 10^{11}$

   Photodissociation reactions are crucial in nuclear astrophysics for creating heavy elements [17]. They break a nucleus into two or more fragments by absorbing a photon.

The *p*-process is a major nucleosynthesis mechanism in explosive stellar events, responsible for generating stable nuclides beyond iron. Photodissociation reactions include those of light nuclei like D, ^{3}He, and ^{7}Li, which can further generate heavier elements.

New technological facilities capable of generating high-intensity and high-resolution γ-ray beams offer new opportunities for astrophysical research [18, 19]. Photodissociation reactions are easier to study than their inverse reactions due to the phase space factor. They occur at energies just above particle emission thresholds.

The main viable option for the moment for particle identification is kinematical identification, requiring high angular and energy resolution. A silicon strip array is the best solution for a dedicated experimental setup [20].

3.1.1 The ELISSA detector array

ELISSA is a collaborative project between LNS-INFN and ELI-NP. It consists of a cylindrical arrangement of 36 position-sensitive detectors, providing approximately 100° of angular coverage. Additional end-cap detectors extend coverage to about 20° (or 160° backward). Figure 3.1 represents a CAD drawing of ELISSA.
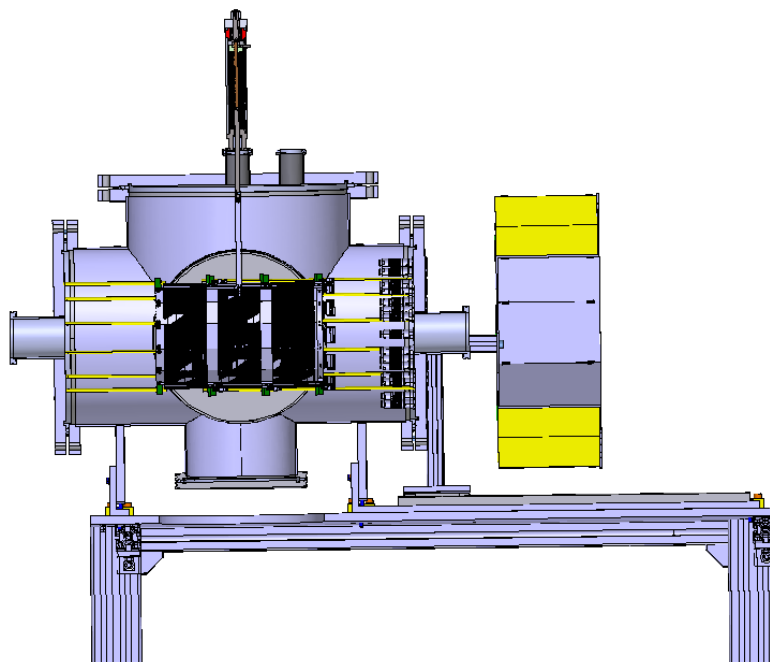
Figure 3.1 CAD rawing of ELISSA silicon strip detection system inside the vaccum chamber.

A simulation of the full array, using VIKAR code, version 4.0 [21], was performed (Figure 3.2). The total efficiency of ELISSA is approximately 90%.
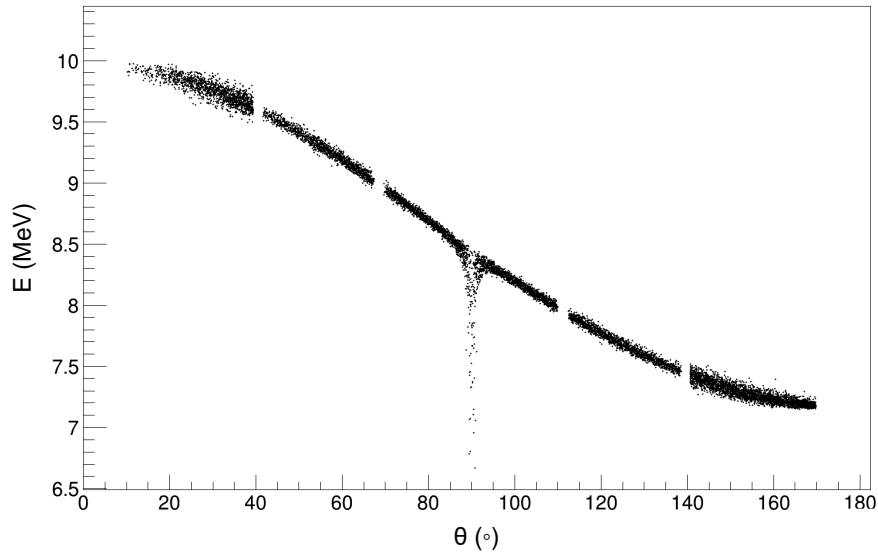
Figure 3.2 Simmulation of ELIISA done using the VIKAR code.

3.2 Silicon detectors at ELI-NP

Silicon detectors rely on p-n junctions, created by introducing different dopant concentrations in a single crystal semiconductor. This creates a charge imbalance and an electric field across the junction, known as the depletion region. Applying a reverse bias to a p-n junction expands the depletion region, increasing the volume for detecting electron-hole pairs generated by incoming radiation. DSSSDs require an electronic chain and a power supply to detect charged particles [22].

3.2.1 PF-16CT-16CD DSSSD

A new test setup for detector electronics was constructed. A DSSSD was used to optimize front-end electronics. Detector-electronics parameters were examined and compared to detector specifications. The front-end electronics and DAQ were fully investigated, considering leakage currents, depletion voltage, and energy resolution [23].

The Mirion Model PF-16CT-16CD DSSSD [24] has 16 back and 16 front strips, with 256 individual 9 mm^2 pixels. The detector was fully depleted at 120 V bias.

A standard two-peak ^{241}Am-^{239}Pu open α-source was positioned in front of the detector at 25 cm. The detector was housed in a vacuum chamber. The energy spectrum is available in Figure 3.3.

The electronic chain consisted of two Mesytec [25] MPR-16 preamplifiers, two Mesytec MSCF-16 shaping/timing filter amplifiers, an Ortec [26] GG8020 gate generator, Mesytec 32 channel Peak Sensing ADC MADC32, and an VME controller SIS3153. The "mvme" DAQ is a user-friendly platform for data acquisition, visualization, and
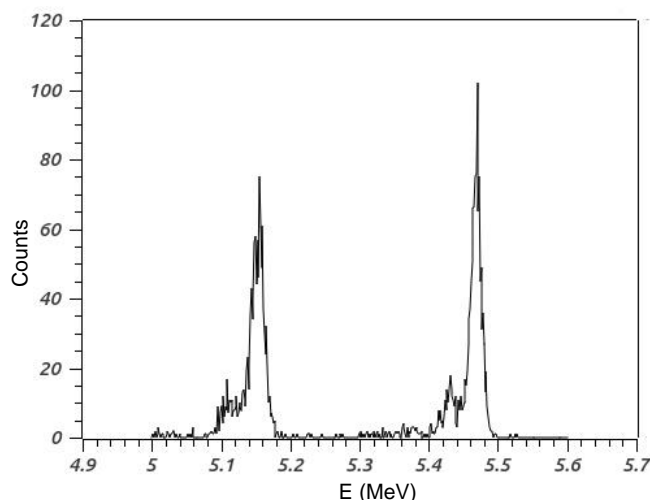
Figure 3.3 Typical energy spectra measured at the front and rear side of the PF-16CT-16CD DSSSD.

basic analysis. **Results and discussion:** The full depletion voltage was determined to be 120 V. The leakage current was measured to be around 0.3 μA (Figure 3.4).

(a)

(b)
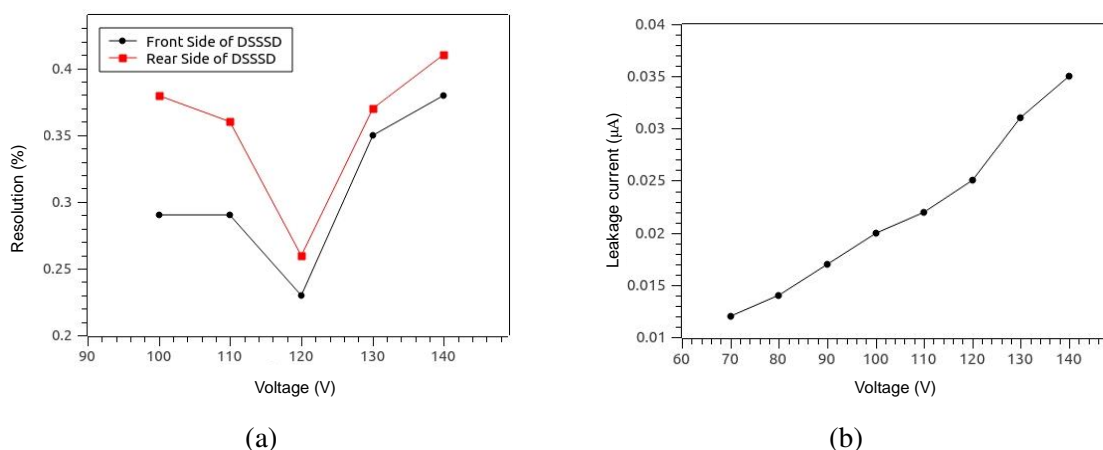
Figure 3.4 (a) Full depletion voltage of the detector at 120 V of the front side of the detector (with black) and the rear side of the detector (with red); (b) Leakage current at different bias values.

Parameters such are pole zero and shaping time were tested and the reuslt is available in Figure 3.5.

The energy resolution obtained on the front side was in the range 0.20% - 0.35%, and on the rear side was 0.24% - 0.39% (Figure 3.6).

In conclusion the test bench for DSSDs was successfully constructed and tested. The Mirion DSSSD model PF-16CT-16CD showed excellent energy resolution and leakage current. The readout chain consisted of Mesytec MPR-16 preamplifiers, MSCF-16 shaping/timing filter amplifiers, GG8020 gate generator, MADC32 ADC, and SIS3153

(a)　　　　　　　　　　　　　　　　(b)
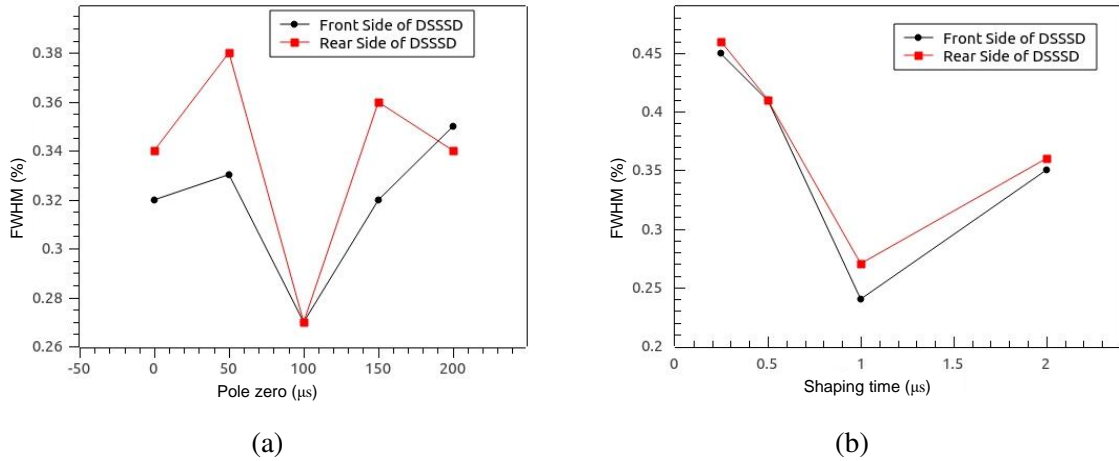
Figure 3.5 (a) The dependence of the energy resolution of the front side (with black) and the rear side of the detector (with red) on pole zero; (b) Dependence of the energy resolution of the front side (with black) and the rear side of the detector (with red) on shaping time.
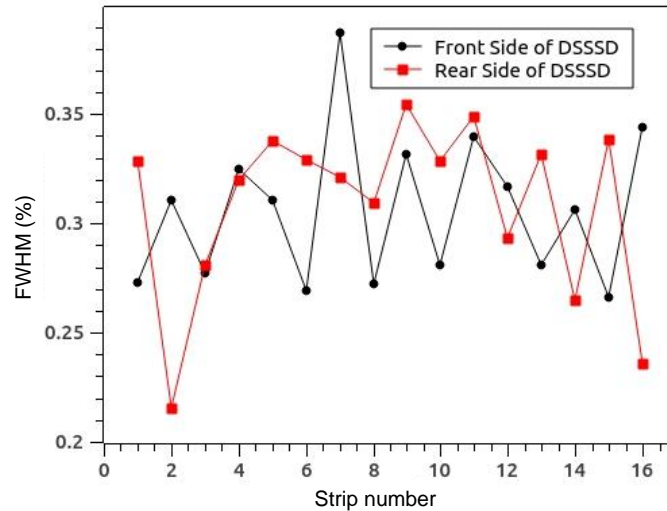
Figure 3.6 The dependence of the energy resolution of the front side (with black) and the rear side of the detector (with red) on the strip number.

VME controller. The "mvme" DAQ provided a user-friendly platform for data acquisition and analysis.

3.2.2　QQQ3 DSSSD

The Micron Model QQQ3 DSSSD [27] has 16 front and 16 back strips, with 256 pixels for x-y position encoding. The thickness is 500 μm or 300 μm. A standard ^{241}Am-^{239}Pu-^{244}Cm three-peak open α-source was positioned in front of the detector at 15 cm. The detector was housed in a vacuum chamber. The electronic chain consisted of two Mesytec MPR-16 preamplifiers, two Mesytec MSCF-16 shaping/timing filter amplifiers, an Ortec GG8020 gate generator, Mesytec 32 channel Peak Sensing ADC MADC32,

and an VME controller SIS3153. Mesytesc mvme DAQ was used for data acquisition.
Typical energy spectrum is available in Figure 3.7.
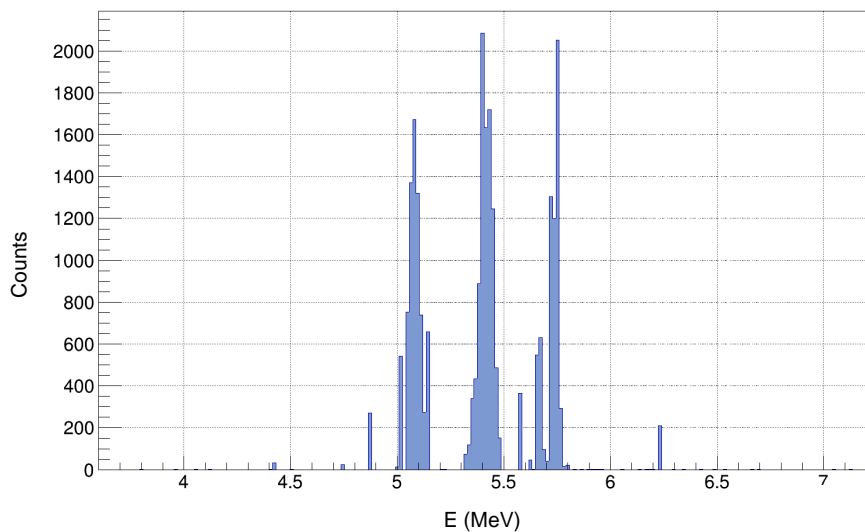
Figure 3.7 Typical energy spectrum measured at the front and rear side of the QQQ3
DSSSD.

QQQ3 DSSSD characteristics are available in Table 3.2:

Table 3.2 QQQ3 DSSSD characteristics

	500 μm	300 μm
Thickness	500 μm	300 μm
Bias	30 V	20 V
Pole zero	100 μs	100 μs
Shaping time	0.5 μs	0.5 μs
Front side energy resolution	30 keV	28 keV
Rear side energy resolution	46 keV	42 keV

3.2.3 X3 PSD

Energy in a PSSSD is determined by:

$$E = Q_1 + Q_2 \tag{3.1}$$

Position in a PSSSD is determined by:

$$P \propto \frac{Q_1 - Q_2}{Q_1 + Q_2} \tag{3.2}$$

where Q_1 and Q_2 is the charge collected at each end (high and low) of the strips.

18

A 1D RC transmission line model can be applied to the resistive strip detector. Charge collection at one contact starts slowly and then rapidly increases. The slowest charge collection occurs at the contact furthest from the impact point [28].

The Micron Model X3 PSD has 4 front resistive strips and 1 back pad. The thickness is 1000 μm.

A standard ^{241}Am-^{239}Pu-^{244}Cm three-peak open α-source was positioned in front of the detector at 15 cm. The detector was housed in a vacuum chamber. The electronic chain consisted of two Mesytec MPR-16 preamplifiers, two Mesytec MSCF-16 shaping/timing filter amplifiers, an Ortec GG8020 gate generator, Mesytec 32 channel Peak Sensing ADC MADC32, and an VME controller SIS3153. Mesytesc mvme DAQ was used for data acquisition.

To calculate the total energy deposited by an α particle, the signal from the upper and lower ends of each strip were summed. Typical energy spectrum is available in Figure 3.8.
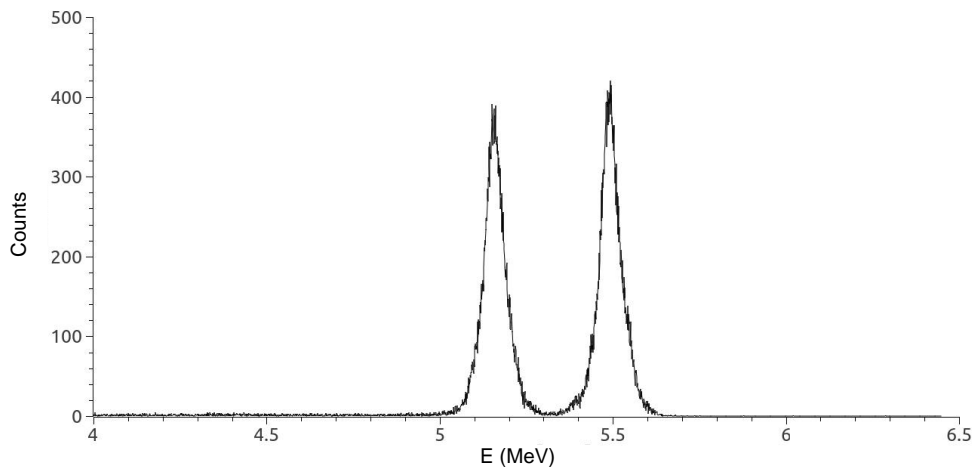
Figure 3.8 Calibrated spectra from X3 PSD detector.

To calibrate position, masks with slit widths of 1 mm were used. A linear transformation was carried out between the position in mm and peak centroids to obtain the calibrated position in mm. The position resolution (FWHM) obtained was approximately 0.3 mm.

In conclusion, the 45 Micron X3 PSD were tested and their overall performances in energy resolution is better than 0.3%. The position resolution of these detectors is below 0.3 mm. These detectors are a great fit for future experiments with charged particles in the exit channel.

Chapter 4

The measurement of $^{19}\text{F}(\text{p},\alpha_0)^{16}\text{O}$ reaction

The low-energy $^{19}\text{F}(\text{p},\alpha)^{16}\text{O}$ reaction has significant implications for nuclear astrophysics. The channels (p,α_0), (p,α_π), and (p,α_γ) are the pathways through which the reaction $^{19}\text{F}(\text{p}, \alpha)^{16}\text{O}$ occurs (Figure 4.1).
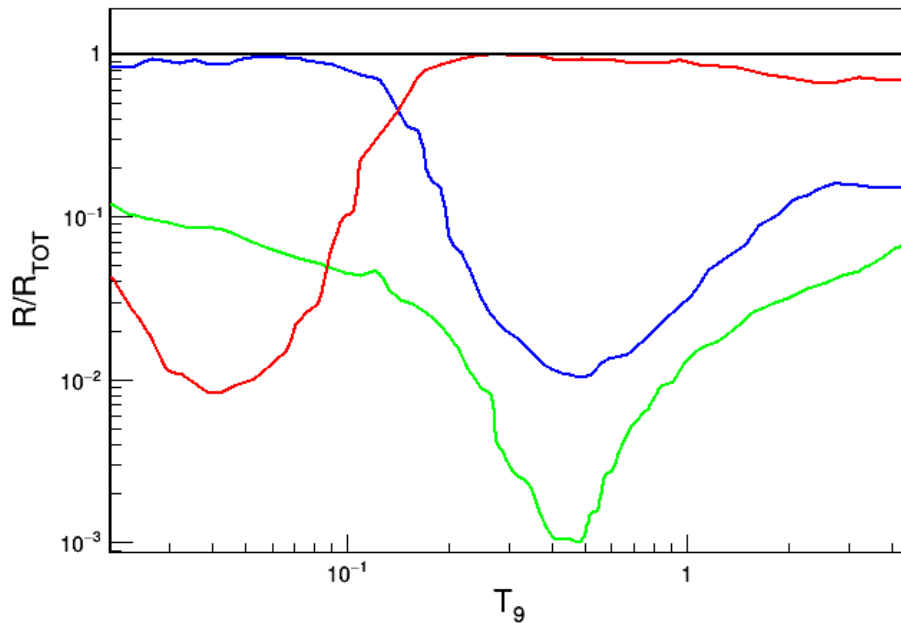
Figure 4.1 Each channel's contribution to the total rate of the reaction.

For temperatures lower than 0.15 GK , the (p,α_0) channel is the dominant contributor of the reaction. The $^{19}\text{F}(\text{p},\alpha_0)^{16}\text{O}$ reaction cross section for energies ranging from 400 to 900 keV was studied in this work. Recent data in the literature reveals a roughly 1.4 increase compared to prior findings reported in the NACRE (Nuclear Astrophysics Compilation of REactions) compilation. Recently, two experimental studies have been reported: the first one measures the *S*-factor between 0.2 MeV and 1 MeV [29], and the

second one uses the Trojan Horse Method (THM) to explore the region of lower energies [30-32]. A summary of the *S*-factors from available literature data for the ^{19}F(p,α)^{16}O reaction is observed in Figure 4.2, indicating a large discrepancy between the most recent data and the previous peaks centered at 681 keV and 738 keV in the center of mass system [29-30, 33-37].
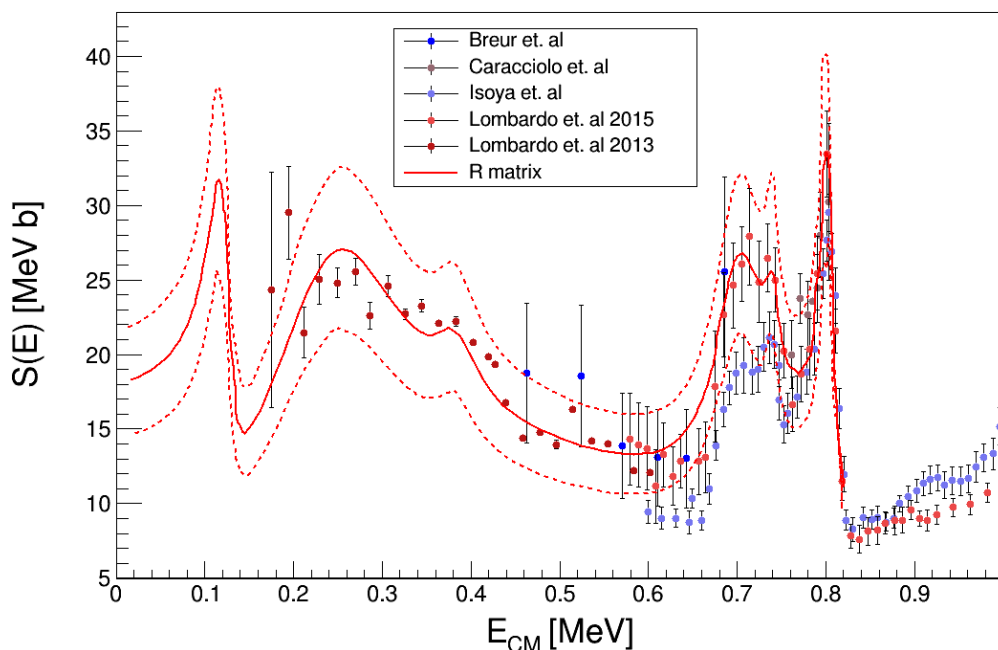
Figure 4.2 *S*-factor of the ^{19}F(p,α_0)^{16}O reaction available in literature (see text for details); taken from [37]

Therefore, we present new additional result of the study published in EPJA employing a silicon strip detector array (LHASA - Large High-resolution Array of Silicon for Astrophysics). The angular distributions, cross sections of the reaction and astrophysical *S*-factors of the (p,α_0) channel were obtained through this experiment. Our findings resolve the discrepancies that exist between the two previously available data sets in the literature.

4.1 Experimental details

The experiment was conducted at INFN Laboratori Nazionali del Sud, Catania (Italy). A ^{19}F beam with energies between 9 and 18.5 MeV was delivered by the 15 MV Tandem Van de Graaff accelerator. Thin self-supported polyethylene targets were positioned at a 90° angle to the beam direction.

The detection setup consisted of six annular single-sided silicon strip detectors mounted in a lamp-shade configuration to form LHASA. LHASA was optimized to

detect α particles from $10°$ to $32°$. A 15 μm thick aluminum shield suppressed fluorine and carbon scattering. The experimental setup is available in Figure 4.3.

Figure 4.3 LHASA - the experimental set-up used for the study of $^{19}F(p,\alpha)^{16}O$ reaction cross section.

Data acquisition was triggered by the total OR of all the strips from the detectors. Signals were processed using charge preamplifiers, programmable amplifiers, and ADCs, and read by an acquisition system for online visualization and data storage.

4.1.1   Beam and target

The beam characteristics are available in Table 4.1:

Table 4.1 Characteristics of the beam and target

E (MeV)	Target thickness (μ g/cm^2)	Charge state	Time (h)	Center of mass energy (keV)
9.0	120	3+	48	408
13.0	115	3+	36	608
14.0	50	3+	24	682
14.5	120	3+	24	689
15.0	100	3+	36	708
16.0	105	4+	18	763
18.5	80	4+	18	896

A collimated monitor detector was used to measure the proton-to-carbon ratio and track target degradation. The detector was calibrated using an α source and positioned at $45°$ relative to the beam (Figure 4.4). A Faraday cup with a suppression voltage was used to measure the beam current. The target was changed every 6-7 hours due to degradation

(Figure 4.5). The monitor detector was also used for normalization, allowing for the calculation of the cross section of interest.
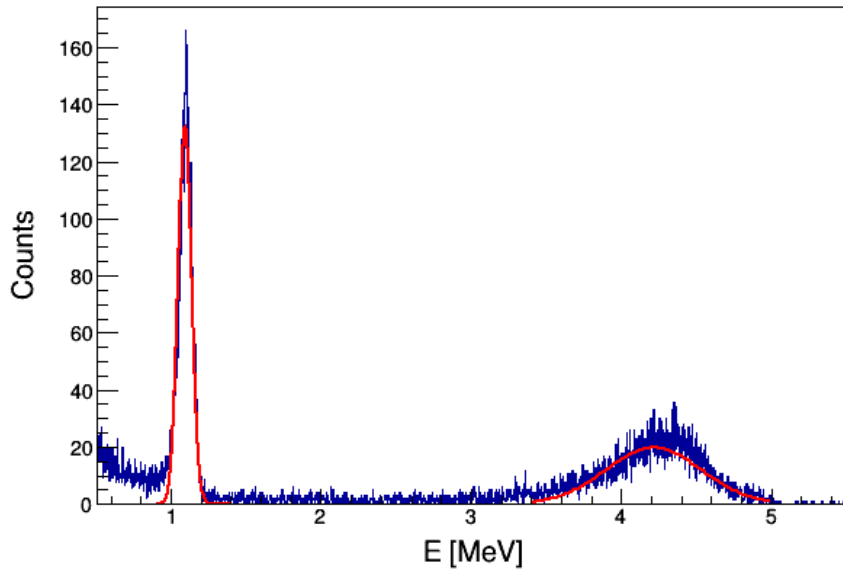
Figure 4.4 Monitor detector spectrum obtained at 15 MeV ^{19}F beam on CH_2 target.
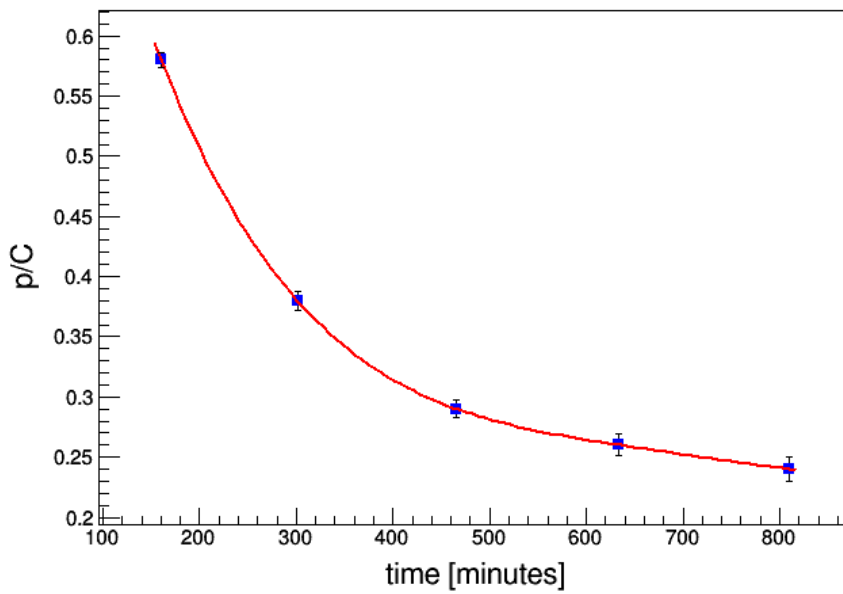
Figure 4.5 Target degradation - proton to carbon ratio over time.

The normalisation procedure is explained below:

$$n = N_{beam}N_{target} = \frac{N_{protons}}{\sigma_{Ruth}\Delta\Omega_m} \tag{4.1}$$

$$\sigma = \frac{N_\alpha}{n\Delta\Omega_s} = \frac{N_\alpha}{N_{protons}}\frac{\Delta\Omega_m}{\Delta\Omega_s}\sigma_{Ruth} \tag{4.2}$$

24

The error of this procedure will depend on the uncertainty in the solid angles of monitor and strips and marginally the statistics.

4.1.2   Set-up

The LHASA detector array, consisting of 6 YY1 silicon strip detectors, was used to measure the $^{19}F(p,\alpha)^{16}O$ reaction cross section. The YY1 detectors, each with 16 strips and a resolution better than 1%, were arranged in a lamp-shade configuration. The detectors were aligned with high precision and their angular coverage was from $10°$ to $32°$.

Figure 4.6 shows the elastic scattering of 12 MeV ^6Li on ^{12}C, confirming the good alignment of the detector. Figure 4.7 illustrates the experimental setup, including the target, detectors, Faraday cup, and monitor detector. The beam traveled from right to left.
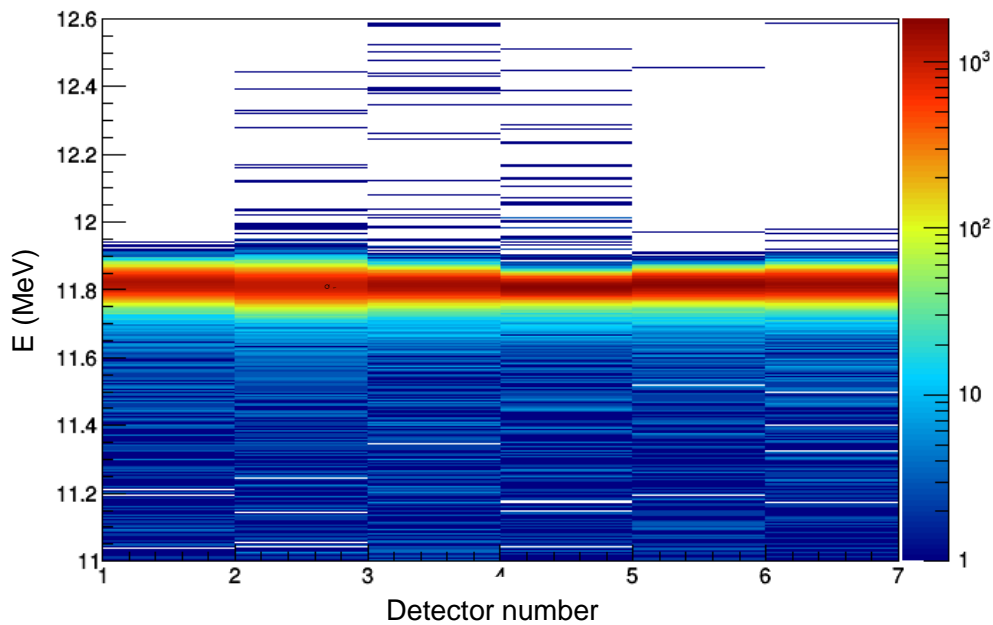
Figure 4.6 Elastic scattering 12 MeV ^6Li beam on ^{12}C target, each bin represents the same strip from all 6 detectors.

4.2   Results

4.2.1   Calibration procedure and simulations

The YY1 detectors were calibrated using ^{228}Th α source and elastic scattering peaks from ^6Li beams on gold and carbon targets. Figure 4.8 shows the calibrated peaks.
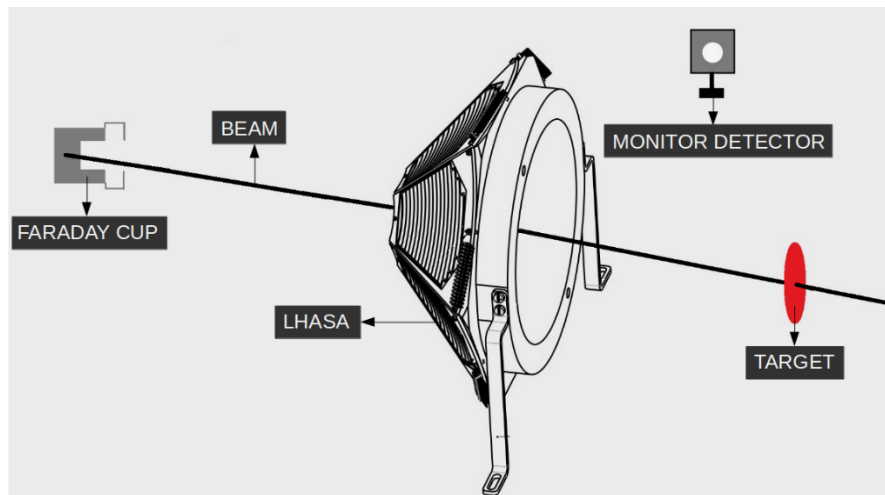
Figure 4.7 LHASA drawing of the the experimental set-up used for the study of ^{19}F(p,α)^{16}O reaction cross section.
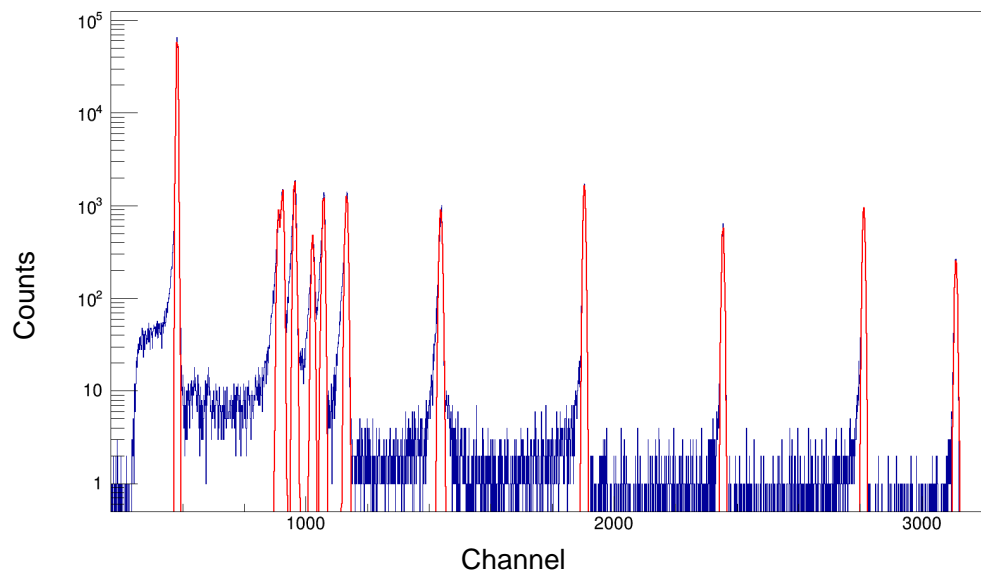
Figure 4.8 Energy calibration of YY1 detectors.

To account for energy losses in the dead layer and target, simulations were performed using LISE++ [38] and GROOT [39]. The excellent agreement between simulated and experimental data for the ^{19}F(p,α_0)^{16}O channel confirms the calibration accuracy. GROOT also verified the detector's circular symmetry. The excellent agreement between symulations and experimental data is available in Figure 4.9

To address the lamp-shade configuration, the experimental data was scaled to a spherical configuration using GROOT simulations.
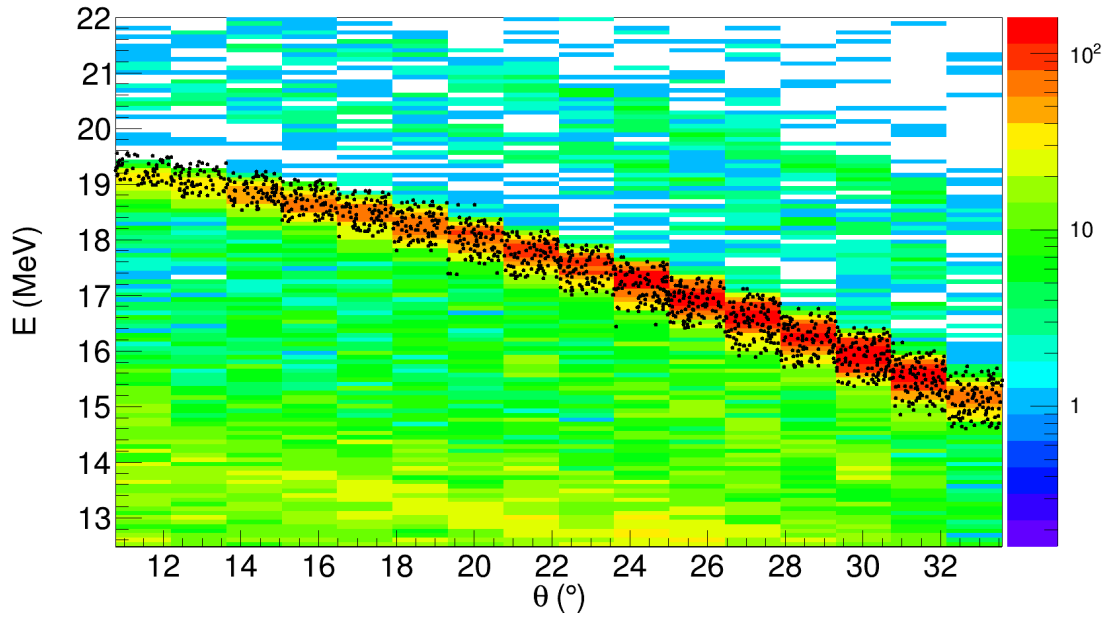
Figure 4.9 Agreement between the simulated data (reported with black dots) and the calibrated experimental points for a beam energy of 18.5 MeV.

4.2.2 Angular distributions

After selecting the $^{19}F(p, \alpha_0)^{16}O$ channel and verifying the coherence of the geometrical placement of the LHASA detector, we extracted the experimental angular distributions and compared them with theoretical calculations for each energy. Our results (Figure 4.10) exhibit slopes that are consistent with those reported in Ref. [29].

Our analysis assumed symmetrical angular distributions, but we expect a stronger asymmetry in non-resonant regions or overlapping resonances due to interference [30]. Experimental data aligns with previous studies, with minor discrepancies. We calculated the total cross section by integrating the Legendre polynomials.

Table 4.2 Legendre polynomials coefficients

E_{CM} (keV)	A_0	A_1	A_2	A_3	A_4
608	0.02105	0.0	-0.00627	0.0	-0.01052
682	0.07024	0.0	0.13085	0.0	0.09818
689	0.08122	0.0	0.15182	0.0	0.15069
708	0.09635	0.0	0.25984	0.0	0.15433
763	0.07996	0.0	0.09878	0.0	0.02895
896	0.08603	-0.03239	-0.01721	0.01984	-0.01053

After the ^{19}F beam interacts with the protons from the CH_2 target, ^{20}Ne is formed in excited state. The increase of the A4 term in the energy range of 0.65-0.75 MeV can be attributed to the excitation of the broad 2^+ state in ^{20}Ne. Similarly, the increase of the A2 term in the same energy range can be attributed to the excitation of 1^- state in ^{20}Ne.

27
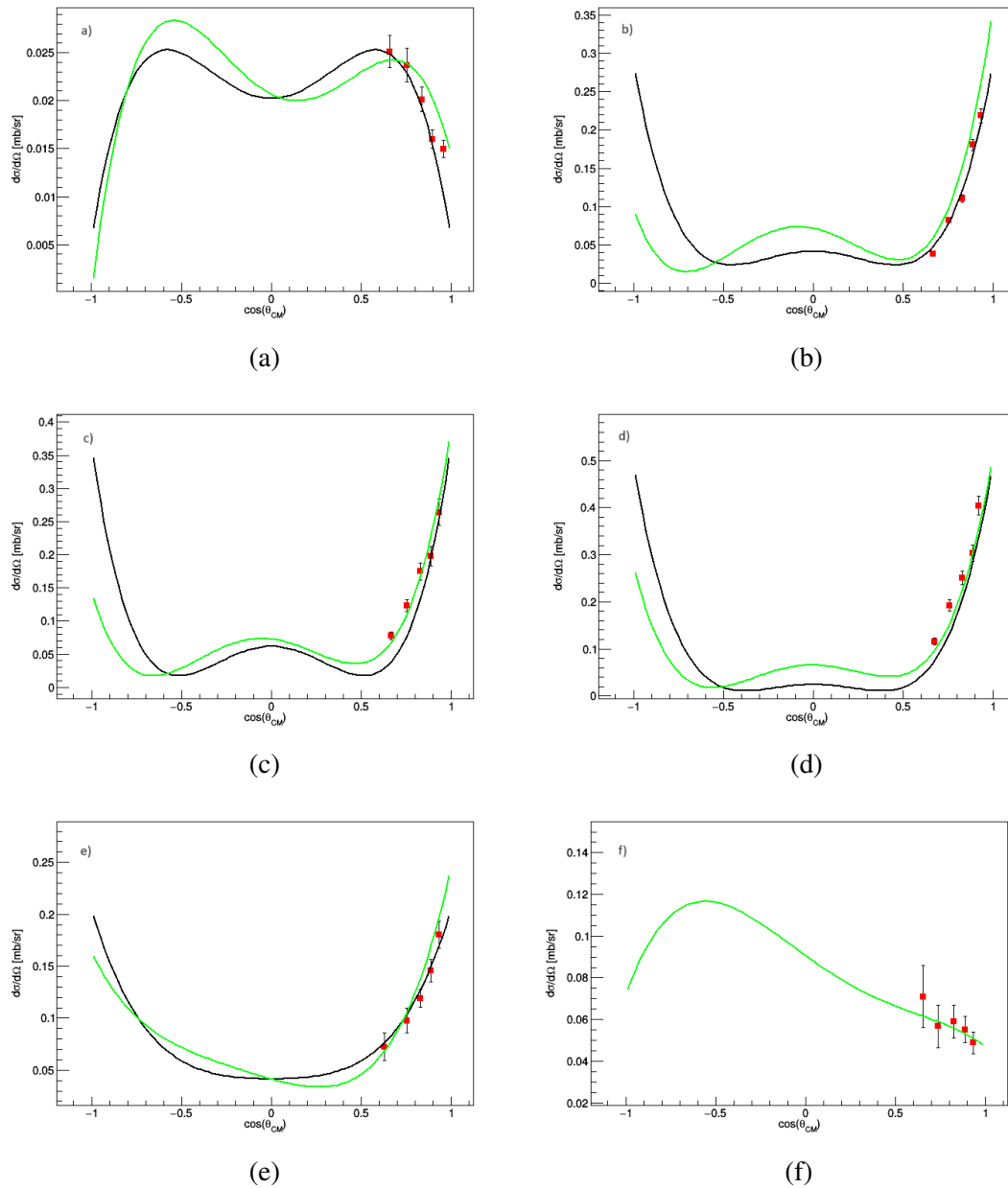
Figure 4.10 Red dots represent experimental points, while and black line represents the best-fit Legendre polynomial to experimental data for the following E_{CM}: (a) 608 keV; (b) 682 keV; (c) 689 keV; (d) 708 keV; (e) 708 keV and (f) 896 keV. Uncertainty in the energy values where evaluated at a maximum of 5 keV The green line represents the Legendre polynomial used by Ref [16].

4.2.3   Cross section and astrophysical *S*-factor

Figure 4.11 (a) shows the *S*-factor of the ^{19}F(p,α_0)^{16}O reaction, already published in Ref. [22] and Figure 4.11 (b) represents the cross section of the ^{19}F(p,α_0)^{16}O reaction. In Figure 4.11 (a), the data from our work is presented by black closed circles, and data taken from previous measurements are presented as follows: red continuous line represents the data of Ref. [30], blue closed circles the data of Ref. [33], light brown

closed circles the data of Ref. [35], light blue closed circles show the data of Ref. [34], light red closed circles represents the data of Ref. [29] and red closed circles show the data of Ref. [36]. In the lower part of Figure 4.11 (b) it is shown the data taken from our work presented by red closed circles, and previous measurements presented as follows: light blue closed circles represents the data of Ref. [21] and blue closed circles show the data of Ref. [16].
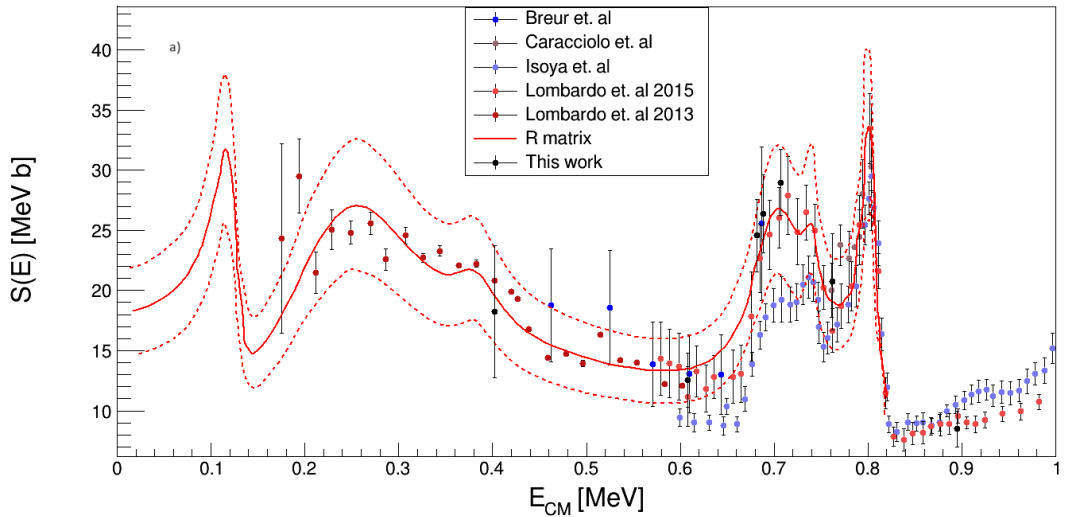
(a)
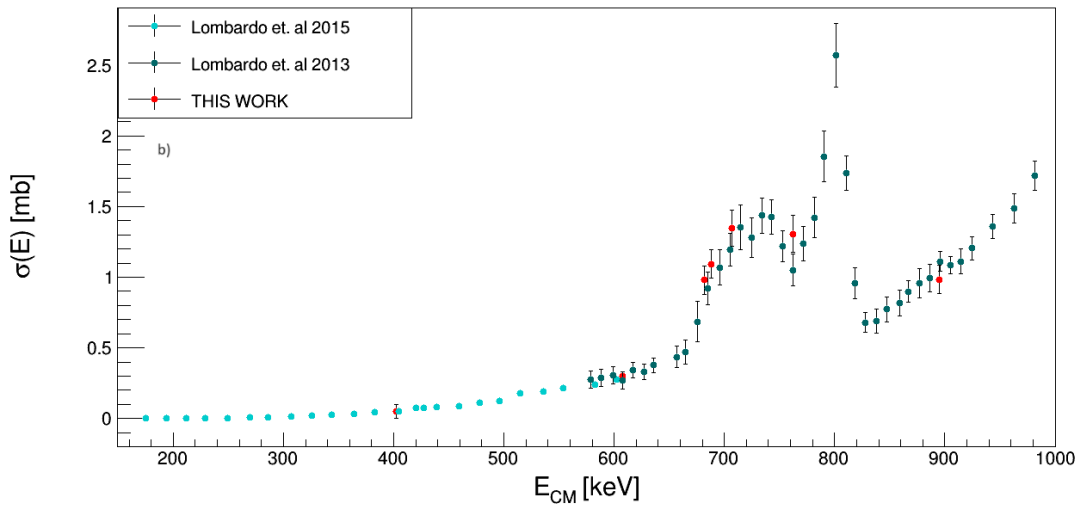
(b)

Figure 4.11 (a) Astrophysical *S(E)*-factor for the ^{19}F(p,α_0)^{16}O reaction measurement (full black points) *vs* data from literature; (b) Cross sections for the ^{19}F(p,α_0)^{16}O reaction measured in the present experiment (full red points) compared with Ref. [29] and Ref. [36].

The error bars of the present data take into account statistical errors, overall systematic errors (including energy calibration and angular integration errors), and uncertainties

due to beam and target particle measurement. The total error of this measurement accounts for 0.5% for the center of mass energy, while the horizontal bars address the total error of 7-8%.

4.3 Conclusions

We measured the cross section of the ^{19}F(p,α)^{16}O reaction, resolving discrepancies with previous data. Our results confirm spin-parity assignments and align with Lombardo's data [ref]. The (p,α_π) and (p,α_γ) channels remain uncertain, requiring further measurements. We propose a new campaign to measure a wider angular range and lower energy range.

Chapter 5

The commissioning of ELISSA detection setup and measurement of ^{19}F(p,α_γ)^{16}O and ^{19}F(p,α_π)^{16}O reactions

5.1 A complete characterization of ELISSA detector array using in-beam data for the first time

The first in-beam tests of the ELISSA experiential setup were conducted using the 3 MV Tandetron accelerator of National Horia Hulubei National Institute for research and development in Physics and Nuclear Engineering (IFIN-HH). During this in-beam performance test, we used both analog and digital electronic modules to process the data. Two different DAQ systems were utilized. The performance of the silicon strip array (such as angular coverage, energy, and position resolution) are detailed in this sub-chapter. We investigated the ELISSA array through simulation, measured energy and position resolution, characterized ballistic deficit, and compared two readout electronic chains and two DAQ systems.

The setup was place inside the small spherical vacuum chamber. Utilizing a preliminary and turbo-molecular pump positioned under the chamber, the experiment was performed with a pressure below 10^{-5} mbar. The vacuum chamber was mounted on the Ion Beam Analysis line.

5.1.1 Experimental details

We used the 3 MV Tandetron accelerator at IFIN-HH to produce ^{7}Li and ^{19}F beams and target them onto carbon and gold. The ELISSA detector ring, consisting of 12 Micron X3 position-sensitive silicon strip detectors, was used to detect the reactions.

The characteristics of the beam, target and electronics are vailable in Table 5.1 and 5.2.

Table 5.1 Characteristics of the beam and the target

Beam	Energy (MeV)	Target	Target thickness ($\mu g/cm^2$)
α source	5.15, 5.68, 5.85	-	-
^{7}Li	7.00, 9.00	Au	149
^{19}F	7.00, 11.00, 13.00, 14.00, 15.00	Au	102
^{19}F	11.00	C	97
^{19}F	11.00	C	97
^{19}F	15.00	CH_2	82

Table 5.2 Type of modules and systems used for data acquisition and processing

Beam	Target	Chain	DAQ
α source	-	Analogue	Mesytec mvme
^{7}Li	Au	Analogue	Mesytec mvme
^{19}F	Au	Analogue	Mesytec mvme
^{19}F	C	Analogue	Mesytec mvme
^{19}F	C	Analogue	DELILA
^{19}F	CH_2	Digital	DELILA

The ELISSA setup was optimized for detecting charged particles in the 35° to 60° angular range. The X3 detectors [27] were 6 cm from the target, and the barrel diameter was 20 cm. Figure 5.1 shows a real image of the setup. We triggered on signals from each strip using both analog and digital chains.
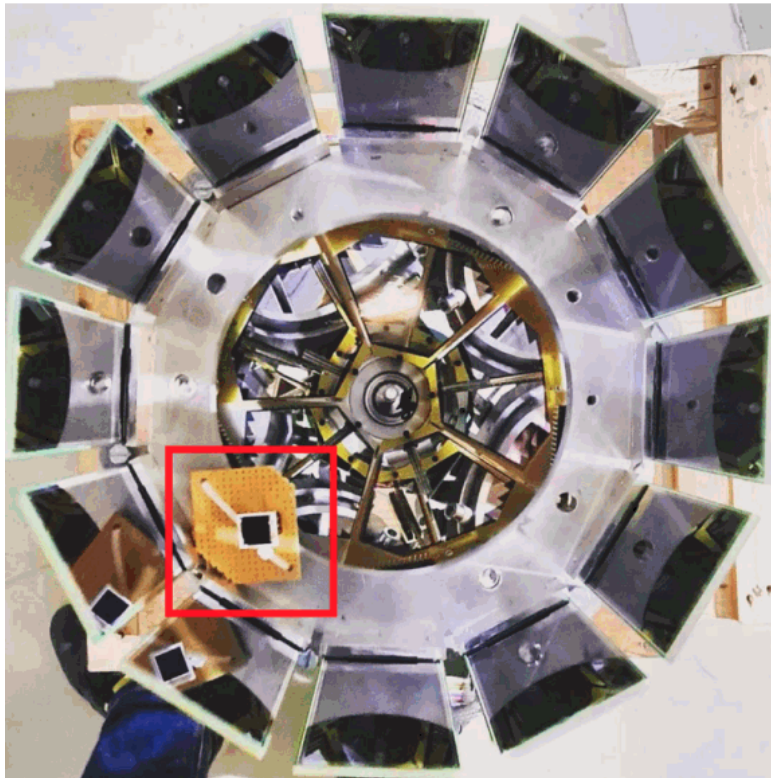

Figure 5.1 Image of the setup used for the first in-beam test.

5.1.2 Electronic chain and data acquisition systems

We tested analog and digital chains. For analog, we used Mesytec hardware [25] and two DAQ systems (Mesytec mvme and DELILA). For digital, we used charge preamplifiers, single-to-differential modules, CAEN 1740 digitizers [40], and a DAQ system.

DELILA, an ELI-NP software, was used for real-time data visualization. It collected data from MADC-32 boards, processed it, and displayed histograms on a web page. DELILA saved data in root files for analysis. Mesytec mvme data was originally saved in '.mvmelst' format, but we converted it to a TTree structure for easier analysis using ROOT.

5.1.3 Energy and position calibration

ELISSA was calibrated using ^{7}Li and a standard 3-peak α source. Gaussian fitting technique was used to determine peak channel numbers and a linear fit to convert them to energy values. The ballistic deficit was corrected by fitting the bands with a quadratic function. ELISSA's energy resolution after the ballistic deficit correction is below 30 keV for 5 MeV α particles. The position was calibrated mounting equally spaced grids in front of the detector. ELISSA's position resolution is below 40 m.

5.1.4 Simulation of the experimental setup

The VIKAR 4.0 code [21] was used to simulate the experimental setup, including geometric efficiency and particle energy losses. The ELISSA detector covered approximately 1.25 sr. For in-beam tests, ^{7}Li and ^{19}F beams were delivered onto a ^{179}Au target. The results of the simulations overlap perfectly with the calibrated experimental data.

5.1.5 Analog *vs* digital DAQ

To compare the DELILA and Mesytec mvme software, 13 MeV ^{19}F beams were delivered onto a ^{12}C target. The Mesytec mvme software demonstrated a better energy resolution (73.9 keV vs. 114.5 keV) than the DELILA software. Comparing the two data sets, it is clear that the energy threshold is lower for the DELILA software, therefore making it a better tool for low energy studies, needed for nuclear astrophysics.

5.1.6 Results

The digital electronic chain enabled us to capture waveforms of the signals, which will be used for future particle identification analysis. Heavier ions, despite shorter travel distances, deposit energy more densely, leading to longer charge collection times due to the weaker electric field in the deeper detector regions. This results in larger rise times for heavier ions compared to lighter ones with the same energy.

During in-beam tests, we detected ^{7}Li, ^{12}C, and ^{19}F particles. We believe that our technique, based on charge collection time, can be used to identify different mass particles. This could be particularly useful in scenarios where traditional ΔE-E measurements are not feasible.

5.2 The measurement of ^{19}F(p,α_γ)^{16}O and ^{19}F(p,α_π)^{16}O reactions

5.2.1 Beam and target

The experiment was conducted at IFIN-HH using a 3 MV Tandetron accelerator to produce a ^{19}F beam. Thin polyethylene targets were placed at 90° to the beam direction. ELISSA, optimized for α particle detection, was positioned 6 cm from the target.

Table 5.1 summarizes the beam energy, target thickness, charge state, and center of mass energy for each measurement.

Table 5.3 Characteristics of ^{19}F beam and target

E (MeV)	Target thickness ($\mu g/cm^2$)	Charge state	E_{CM} (keV)
9	90	3+	420
10	90	3+	480
11	60	4+	530
12	100	4+	580
13	70	4+	625
14	50 and 150	5+	680
15	50	5+	730

An on-line monitoring system, using a detector placed at 30°, was employed to monitor the target. The detector was calibrated using ^{7}Li beams scattered on a gold target. A Faraday cup was used to measure the beam current, and the reaction chamber was maintained under high vacuum.

The target degradation was monitored by observing the proton-to-carbon ratio. The monitor detector was also used for normalization. The cross section was calculated using the detected particles, solid angles, and Rutherford cross section.

5.3 Selection of the reaction channel

The dataset underwent a selection process to select the channel of interest. LISE++ simulations (Figure 5.2) were used to verify the channel selection.

The black line in Figure 5.2 represents ^{12}C from elastic scattering, the pink line represents ^{19}F from elastic scattering, and the red lines represent the expected α particles from the ^{19}F(p, α)^{16}O reaction.
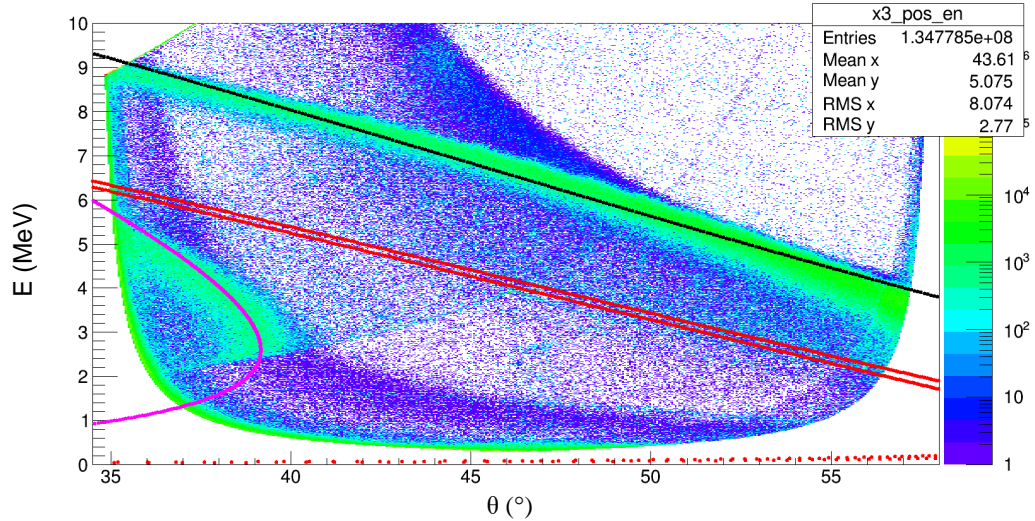
Figure 5.2 15 MeV ^{19}F beam on CH_2 target. The experimental data is overlapped with
LISE++ simulations.

After selecting the energy region of interest, the two channels are separated for
further analysis, including angular distribution and cross section calculations.

5.4 Conclusions

The ELISSA detector array, developed at ELI-NP in collaboration with INFN-LNS, was
tested at the 3 MV Tandetron accelerator. The array's energy resolution was found to be
0.35% for α particles. In-beam tests with various particles showed a correlation between
particle mass and energy resolution, with heavier particles having smaller resolution.

Two DAQ systems and two electronic chains were compared. The analogue chain
performed better overall, but the digital chain offers the advantage of waveform analysis
for particle identification.

Simulations using VIKAR [21] and LISE++ [38] were crucial for accurately deter-
mining the reaction channel of interest, especially given the close energy separation
between (p, α_π) and (p, α_γ) channels.

Conclusions and Perspectives

AGB stars are key contributors to the production of elements in the Universe. Due to their thermal pulses and dredge-up events, they can provide the necessary conditions for fluorine nucleosynthesis. While the production of many elements is well-understood, the origin of fluorine remains not completely understood. In order to solve this puzzle, a combination of theoretical modeling, laboratory experiments, and high-precision astronomical observations is required. Accurate determination of thermonuclear reaction rates is essential for modelling stellar nucleosynthesis. The Gamow peak has an important role in shaping the energy window for thermonuclear reactions. The R-matrix theory, while complex, provides a robust framework for describing compound nuclear reactions.

Future research should focus on improving experimental techniques to measure cross sections at astrophysically relevant energies. This thesis presents charged particles detector development and characterization, with a specific focus on the field of nuclear astrophysics (low energy, low treshold). The successful implementation and testing of a DSSSD test bench at ELI-NP marked a significant milestone, demonstrating the detector's exceptional performance in terms of energy resolution. These findings show its suitability for the experimental conditions. The ELISSA array, a key component of future experiments, shows promising characteristics in terms of energy resolution, position resolution, low threshold and maybe even particle identification.

An important contribution of this work lies in solving the discrepancy between the last available data in the literature and the previous data reported in the NACRE compilation, for the ^{19}F(p,α_0)^{16}O reaction cross section. The results are in agreement with previous assignments of spin-parity of the resonances situated at 681 keV and 738 keV in the center-of-mass system, which is due to the population of the 13.529 MeV and 13.586 MeV excited levels of ^{20}Ne. This experiment paves the way for future investigations targeting the less well-constrained $^{19}F(p, \alpha_\pi)^{16}$O and $^{19}F(p, \alpha_\gamma)^{16}$O channels.

The ELISSA detector array provided the necessary energy resolution for the study of $^{19}F(p, \alpha_\pi)^{16}$O and $^{19}F(p, \alpha_\gamma)^{16}$O reaction channels. By carefully calibrating the detectors and implementing data selection criteria, we have established a solid foundation for extracting meaningful results from the collected data.

In the end, this research advances our understanding of fluorine nucleosynthesis in AGB stars by developing advanced detector systems and conducting precise measurements of the ^{19}F(p,α)^{16}O reaction cross section.

Conclusions and Perspectives

The study of fluorine production in AGB stars is a field with many opportunities for advancement. Building upon the strong foundation established in this research, future analysis will focus on determining the angular distributions for the (p,α_π) and (p,α_γ) reaction channels. Afterwards, the cross section will be calculated for both $^{19}F(p,\alpha_\pi)^{16}O$ and $^{19}F(p,\alpha_\gamma)^{16}O$ reaction cross sections.

Expanding the ELISSA array and developing novel detector technologies will be very important in improving data quality and precision. Solutions like the use of Mesytec model MMM detectors, or coupling ELISSA array with γ-ray detectors will pave the way for new experiments in the field of nuclear astrophysics.

Bibliography

[1] V. Liccardo, *Production of chemical elements in Astrophysics*, DOI: 10.13140/RG.2.1.1977.8005, 2015

[2] E. M. Burbidge, et al., *Synthesis of the elements in stars*, Reviews of Modern Physics, 29:547–650, 1957

[3] website, https://en.m.wikipedia.org/wiki/File:Evolution-of-a-Sun-like-star.svg, accessed on 03.18.2024

[4] F. LeBlanc, *An Introduction to Stellar Astrophysics*, book, 2010.

[5] M. Lugaro, *Stardust from meteorites. An introduction to presolar grains*, September 2005.

[6] F. Herwi *Evolution of Asymptotic Giant Branch Stars*, Annual Review of Astronomy and Astrophysics, 43:435–479, September 2005

[7] R. J. De Boer. *PhD thesis*, University of Notre Dame, 2011.

[8] S. E. Woosley and W. C. Haxton, *Supernova Neutrinos, Neutral Currents and the Origin of Fluorine*, Nature, 334:45–47, 1988.

[9] G. Meynet and M. Arnould, *Synthesis of 19F in Wolf-Rayet stars*, 355:176–180, 2000.

[10] A. Jorissen, et al., *Fluorine in red giant stars - Evidence for nucleosynthesis*, Astronomy and Astrophysics, 261:164–187, 1992.

[11] C.E. Rolfs and W.S. Rodney, *Cauldrons in the Cosmos* 1988, book.

[12] D. D. Clayton, *Principles of stellar evolution and nucleosynthesis* 1983, book.

[13] C. Iliadis, *Nuclear Physics of Stars*, 2007, book.

[14] G. Gamow, *Zur Quantentheorie des Atomkernes*, Zeitschrift fur Physik, 51:204–212, March 1928.

[15] G.A. Mourou et al., *ELI–Extreme Light Infrastructure Science and Technology with Ultra-Intense Lasers Whitebook*, THOSS Media GmbH, 2011.

[16] P. Constantin et al., *Design concept of a g-ray beam with low bandwidth and high spectral density*, Phys. Rev. Accel. Beams, 27:021601, 2024

[17] C. Iliadis, *Nuclear Physics of Stars*, Wiley-VCH Verlag, 2007.

[18] D.L. Balabanski et al., *New light in nuclear physics: The extreme light infrastructure*, Europhysics Letters, 117:28001, 2017.

[19] D. Filipescu et al., *Perspectives for photonuclear research at the Extreme Light Infrastructure - Nuclear Physics (ELI-NP) facility*, Eur. Phys. J. A, 51: 185, 2015.

[20] D. Lattuada et al., *A fast and complete GEANT4 and ROOT Object-Oriented Toolkit: GROOT*, EPJ Web Conf., 165:01034, 2017.

[21] S.D. Pain, VIKAR code, https://sites.google.com/a/nuclearemail.org/vikar/ version 4.0.

[22] A. Guinier and R. Jullien, *The Solid State*, Oxford University Press, pg 115-116, 1989.

[23] T. Petruse, et al., *Test bench for silicon strip detectors: front-end electronics and DAQ*, U.P.B. Sci. Bull., Series A, Vol. 82, Iss. 3, 2020.

[24] Mirion, General catalogue, http://www.mirion.com.

[25] Mesytec, General catalogue, http://www.mesytec.com.

[26] Ortec, General catalogue, https://www.ortec-online.com.

[27] Micron Semiconductor Ltd, https://www.micronsemiconductor.co.uk.

[28] Andrew Robinson, *Properties of Position Sensitive Silicon Strip Detector's*, Department of Physics, University of Surrey, master thesis.

[29] I. Lombardo et al., *Toward a reassessment of the $^{19}F(p,\alpha_0)^{16}O$ reaction rate at astrophysical temperatures*, Physics Letters B, 748:178–182, 2015.

[30] I. Indelicato et al., *New Improved Indirect Measurement of the $^{19}F(p, \alpha)^{16}O$ Reaction at Energies of Astrophysical Relevance*, Astrophys. J., 845:19, 2017.

[31] M. La Cognata et al., *The Fluorine Destruction In Stars: First Experimental Study Of The $^{19}F(p,\alpha_0)^{16}O$ Reaction At Astrophysical Energies*, ApJL, 739:L54, 2011.

[32] A. Tumino et al., *The Trojan Horse Method: A Nuclear Physics Tool for Astrophysics*, Annu. Rev. Nucl. Part. Sci., 71:345–376, 2021.

[33] G. Breuer, *Messung und Analyse von Winkelverteilung und Wirkungsquerschnitt der Reaktion $^{19}F(p,\alpha_0)^{16}O$ im Energiebereich 0,4 bis 0,72 MeV*, Z. Physik, 154:339–351, 1959.

[34] A. Isoya et al., *The angular distributions of the long-range alpha-particles from the reaction $^{19}F(p,\alpha_0)^{16}O$*, Nuclear Physics A, 7:116, 1958.

[35] R. Caracciolo et al., *The 13.645 MeV state in 20Ne*, Lett. Nuovo Cimento, 11:33–38, 1974.

[36] I. Lombardo et al., *Analysis of the $^{19}F(p,\alpha_0)^{16}O$ reaction at low energies and the spectroscopy of ^{20}Ne*, J. Phys. G: Nucl. Part. Phys., 40:125102, 2013.

[37] G.L. Guardo et al., *Direct measurement of the $^{19}F(p,\alpha_0)^{16}O$ reaction at E_{cm}= 0.4–0.9 MeV using the LHASA detector array*, The European Physical Journal A, 59:65, 2023.

[38] https://lise.nscl.msu.edu/lise.html.

[39] D. Lattuada et al., *A fast and complete GEANT4 and ROOT Object-Oriented Toolkit: GROOT*, EPJ Web Conf., 165:01034, 2017.

[40] https://www.caen.it/caen-digitizer-whitepaper/